ORIGINAL SCIENTIFIC PAPER OPEN ACCESS

A pseudo-rigid-body approach for determination of parasitic displacements of lumped compliant parallel-guiding mechanisms

Slaviša Šalinić[1*]

[1]University of Kragujevac, Faculty of Mechanical and Civil Engineering in Kraljevo, Kraljevo, Serbia

ARTICLE INFO

[*] **Correspondence:** salinic.s@mfkv.kg.ac.rs

DOI: 10.5937/engtoday2300008S

UDC: 621(497.11) **ISSN:** 2812-9474

Article history: Received 3 June 2023; Revised 5 July 2023; Accepted 8 July 2023

ABSTRACT

Parasitic displacements of a guiding plate of a lumped compliant parallel-guiding mechanism are analyzed using the pseudo-rigid-body (PRB) approach. Small deformations of flexure hinges are assumed. Each flexure hinge of the compliant mechanism is modelled by the PRB model with 3-DOF (degrees of freedom). This model allows that axial deformation of the flexure hinge to be considered. The corresponding expressions in symbolic form for both translational and rotational parasitic displacements of the compliant mechanism are derived. The obtained expressions enable the analysis of the influence of various structural parameters as well as various types of flexure hinges on the parasitic displacements of the considered type of compliant parallel-guiding mechanisms.

KEYWORDS

Pseudo-rigid-body model, Compliant mechanisms, Parasitic displacements, Quasi-static, Flexure hinge

1. INTRODUCTION

The compliant mechanisms are widely used in many industrial applications such as micro/nano positioning and measuring, energy harvesting, micro vibration suppression etc. (see e.g. [1-5]). Today, kinetostatic and dynamics analyses of this type of mechanisms represent an attractive scientific research field. Unlike classic mechanisms, where the transfer of forces and displacements between the members of the mechanism is realized through classic joints, in compliant mechanisms it is realized by means of flexure hinges. In this way, the unwanted effects of friction, bucklash, and wear, which always appear during the exploitation of mechanisms with classic joints, were avoided. In the literature, various procedures have been developed for kinetostatic and dynamic analyses of compliant mechanisms such as the transfer matrix method [6-10], the dynamic stifness method [11,12], the beam theory based method [13-15], the pseudo-rigid-body model [16-20], the finite element method [21-23], the multi-compliant-body matrix method [24], the compliance matrix method [25-27], the Castigliano's second theorem based method [28], the unit-load method [29] etc. A survey of results, methods, and ongoing problems in compliant mechanisms research field was given in [30].

In this paper the problem of analysis of parasitic displacements occurring in lumped compliant parallel-guiding mechanisms are considered. Previously in the literature, this problem was discussed in papers [31-33]. The analysis of parasitic displacements in spatial complaint mechanisms was given in [34]. However, in papers [31-33] the considerations were limited only to the leaf spring type of flexure hinges in the frame of Euler-Bernoulli beam theory. In this paper, the flexure hinges of variable thickness with both transverse and axial symmetry axes are considered. Using the pseudo-rigid-body (PRB) approach derived in [17], the corresponding expressions for parasitic

displacements of the considered compliant parallel mechanism are derived. The influence of both various geometrical parameters of the compliant mechanism and various shapes of flexure hinges on the mechanism parasitic displacements is examined.

2. PRB MODEL OF THE LUMPED COMPLIANT PARALLEL-GUIDING MECHANISM

2.1. Model 1

Consider a lumped compliant parallel-guiding mechanism shown in Fig. 1. The corresponding geometric parameters of the compliant mechanism are indicated in Fig. 1. The out-of-plane width w of the compliant mechanism is constant.

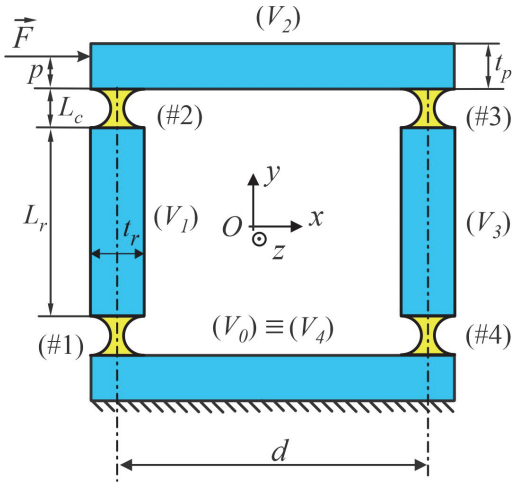

Figure 1: A lumped compliant parallel-guiding mechanism

The compliant mechanism is composed of four identical flexure hinges with variable thicknesses and of four rigid beams. The geometric parameters of the flexure hinges are shown in Fig.2 where $t_c = t(\xi = L_c/2)$ represents the minimal value of the flexure hinge thickness.

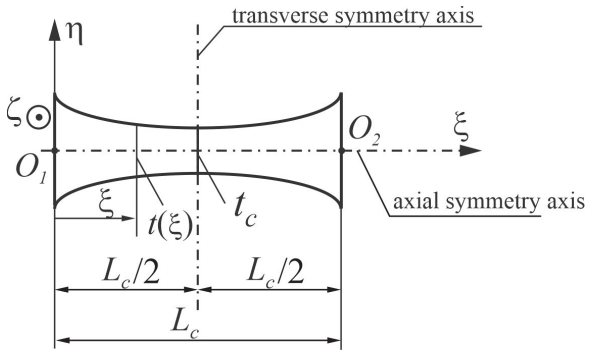

Figure 2: Geometry parameters of flexure hinges

In Fig. 2, the inertial frame $O_1\xi\eta\zeta$ is fixed at the left end O_1 of the flexure hinge where the $\xi-$ axis coincides with the neutral axis of the flexure hinge in its undeformed configuration and the axes η and ζ represent the principal axes of the flexure rectangular cross-section. It is assumed that the flexure hinges have both transverse and axial symmetry axes. The flexure hinges are denoted by (#1), (#2), (#3), and (#4) whereas the rigid beams are denoted by (V_1), (V_2), (V_3), and $(V_4) \equiv (V_0)$. The rigid body (V_2) represents the guiding plate of the parallel-guiding mechanism and the left and the right supporting arm of the mechanism are formed of the elements (V_1), (#1), and (#2) as well as of (V_3), (#3), and (#4), respectively. It is assumed that the flexure hinges perform small plane deformations in the plane Oxy of the inertial frame $Oxyz$. In addition, the guiding plate is exposed to a horizontal force $\vec{F}$ of a magnitude equals $2F$. Note that, in [31] the rigid body (V_1) is fixed instead of the body (V_0) and force $\vec{F}$ has the vertical direction acting on the top surface of the guiding plate (V_2). In this paper, the PRB approach is used in the kinetostatic analysis of the considered compliant mechanism. In the PRB approach a flexure hinge is replaced by two massless rigid links interconnected by a joint with either one degree of freedom or three degrees of freedom (DOF) as it is shown in Fig. 3.

The stiffnesses k_{L1}, k_{L2}, and k_R indicated in Fig. 3 are determined by the following expressions [17]:

$$k_R = \frac{1}{C_{b,r}}, \quad k_{L1} = \frac{1}{C_a}, \quad k_{L2} = \frac{C_{b,r}}{\left[C_{b,t} + 2\alpha_f C_a (1+\mu)\right] C_{b,r} - L^2 C_{b,r}^2 / 4}, \tag{1}$$

where $\alpha_f = 1/k_s$ is the correction factor, $k_s = 5/6$ is the shear coefficient for rectangular cross-section, μ is Poisson's coefficient, and finally C_a, $C_{b,t}$, and $C_{b,r}$ are axial, bending translatory and bending rotary compliances, respectively. In according to the Castigliano's second displacement theorem [5,27], these compliances are determined by the following expressions:

$$C_a = \frac{1}{Ew}\int_0^{L_c} \frac{d\xi}{t(\xi)}, \qquad C_{b,t} = \frac{12}{Ew}\int_0^{L_c} \frac{\xi^2 d\xi}{t(\xi)^3}, \qquad C_{b,r} = \frac{12}{Ew}\int_0^{L_c} \frac{d\xi}{t(\xi)^3}, \tag{2}$$

where E is the elasticity modulus of the compliant mechanism. The closed-form expressions of these compliance coefficients for various types of flexure hinges can be found, for example, in [3,5]. In accordance to [27], for the short flexure hinges with a length to depth ratio of less than 5, that is $L_c < 5\max(t(\xi), w)$, it should be taken that $\alpha_f \neq 0$.

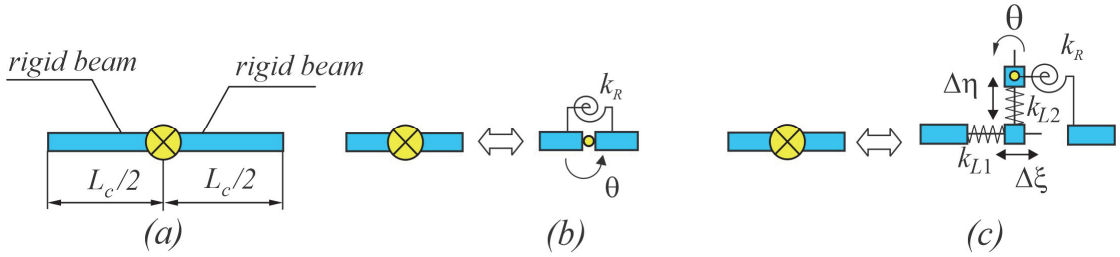

Figure 3: (a) PRB model of a flexure hinge; (b) model with 1-DOF joint; (c) model with 3-DOF joint

The 1-DOF PRB model of a flexure hinge is developed in [1] whereas the 3-DOF PRB model is presented in [17]. The main drawback of 1-DOF PRB model is that it cannot cover either the effect of the axial loading of the flexure hinge or the effect of shearing produced by the transverse loading of the flexure hinge. So, in this paper, 3-DOF PRB model of the flexure hinges developed in [17] is used. Application of the 3-DOF PRB model approach [17] to the general planar flexure-based compliant mechanism yields the corresponding planar rigid multibody system as it is shown in Fig. 4.

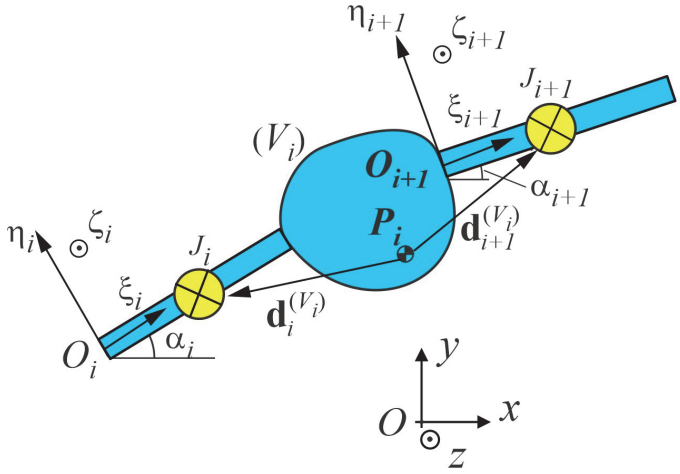

Figure 4: PRB model of a general planar flexure-based compliant mechanism

Here, P_i represents an arbitrarily chosen point on the rigid body (V_i), $O_i\xi_i\eta_i\zeta_i$ is the flexure hinge inertial frame where the axis ξ_i coincides with the undeformed rectilinear axis of the flexure hinge (#*i*), and α_i is the angle between the axis ξ_i and the axis x in the undeformed configuration of the compliant mechanism. More details on this modelling technique can be found in [17]. Applying this modelling technique to the lumped compliant parallel-guiding mechanism considered yields its PRB model shown in Fig. 5.

The geometric parameters corresponding to the PRB model derived read as follows:

$$\alpha_1 = \alpha_2 = \pi/2, \quad \alpha_3 = \alpha_4 = -\pi/2, \tag{3}$$

$$\mathbf{d}_1^{(V_1)} = [0, -\frac{L_r}{2} - \frac{L_c}{2}, 0]^T, \quad \mathbf{d}_2^{(V_1)} = [0, \frac{L_r}{2} + \frac{L_c}{2}, 0]^T, \quad \mathbf{d}_2^{(V_2)} = [\frac{t_r}{2}, -\frac{L_c}{2} - p, 0]^T, \tag{4}$$

$$\mathbf{d}_3^{(V_2)} = [\frac{t_r}{2} + d, -\frac{L_c}{2} - p, 0]^T, \quad \mathbf{d}_3^{(V_3)} = [0, \frac{L_r}{2} + \frac{L_c}{2}, 0]^T, \quad \mathbf{d}_4^{(V_3)} = [0, -\frac{L_r}{2} - \frac{L_c}{2}, 0]^T. \tag{5}$$

For each of the points $P_i\,(i=1,\ldots,4)$, the corresponding active external loads vector can be associated as follows:

$$\mathbf{F}_1 = \mathbf{F}_3 = [0, 0, 0]^T, \quad \mathbf{F}_2 = [2F, 0, 0]^T. \tag{6}$$

The external horizontal force $\vec{F}$ produces small planar elastic deformations of the flexure hinges yilding displacements of the points $P_i\,(i=1,\ldots,3)$ relative to undeformed configuration of the compliant mechanism described by the following vectors:

$$\mathbf{u}_{P_i} = [u_{ix}, u_{iy}, 0]^T, \ i=1,\ldots,3, \tag{7}$$

as well as rotations $\theta_i\,(i=1,\ldots,3)$ of the rigid bodies $(V_i)(i=1,\ldots,3)$ (the anticlockwise rotation is used as the positive direction of these angles), respectively to which the following vectors can be associated:

$$\mathbf{\Theta}_i = [0, 0, \theta_i]^T, i=1,\ldots,3. \tag{8}$$

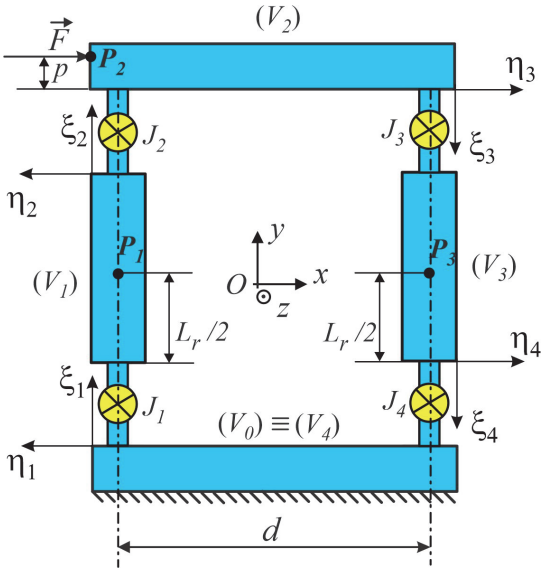

Figure 5: PRB model (model 1) of the lumped compliant parallel-guiding mechanism

Also, the relative rotational displacements and the vectors of relative translatory displacements at the joints $J_i\,(i=1,\ldots,4)$ expressed in the local frames $O_i\xi_i\eta_i\zeta_i\,(i=1,\ldots,4)$ read as follows:

$$\Delta\theta_i = \theta_i - \theta_{i-1}, \quad \mathbf{u}_{J_i} = [\Delta\xi_i, \Delta\eta_i, 0]^T, \ i=1,\ldots,4, \tag{9}$$

where $\theta_0 = \theta_4 = 0$ (see Fig. 5). Based on [17], the vectors $\mathbf{u}_{J_i}\,(i=1,\ldots,4)$ are determined by the following expressions:

$$\mathbf{u}_{J_1} = \mathbf{u}_{P_1} + \widetilde{\mathbf{\Theta}}_1 \mathbf{d}_1^{(V_1)}, \tag{10}$$

$$\mathbf{u}_{J_j} = \mathbf{u}_{P_j} + \widetilde{\mathbf{\Theta}}_j \mathbf{d}_j^{(V_j)} - \mathbf{u}_{P_{j-1}} - \widetilde{\mathbf{\Theta}}_{j-1} \mathbf{d}_j^{(V_{j-1})}, \ j=2,3, \tag{11}$$

$$\mathbf{u}_{J_4} = -\mathbf{u}_{P_3} - \widetilde{\mathbf{\Theta}}_3 \mathbf{d}_4^{(V_3)}, \tag{12}$$

where $\widetilde{\mathbf{\Theta}}_i$ is the skew-symmetric matrix associated with the vector $\mathbf{\Theta}_i$ and where components of the vector $\mathbf{d}_i^{(V_j)}$ and the matrix $\widetilde{\mathbf{\Theta}}_i$ with respect to the inertial frame *Oxyz* are given by:

$$\mathbf{d}_i^{(V_j)} = [d_{ix}^{(V_j)}, d_{iy}^{(V_j)}, 0]^T, \tag{13}$$

$$\widetilde{\mathbf{\Theta}}_i = \begin{bmatrix} 0 & -\theta_i & 0 \\ \theta_i & 0 & 0 \\ 0 & 0 & 0 \end{bmatrix}^T. \tag{14}$$

Now, based on the expressions (7)-(9), (13), and (14), the coordinate forms of the matrix expressions (10)-(12) read:

$$\begin{bmatrix}\Delta\xi_1\\ \Delta\eta_1\\ 0\end{bmatrix}=\mathbf{A}_1\left(\begin{bmatrix}u_{1x}\\ u_{1y}\\ 0\end{bmatrix}+\begin{bmatrix}-\theta_1 d_{1y}^{(V_1)}\\ \theta_1 d_{1x}^{(V_1)}\\ 0\end{bmatrix}\right), \tag{15}$$

$$\begin{bmatrix}\Delta\xi_j\\ \Delta\eta_j\\ 0\end{bmatrix}=\mathbf{A}_j\left(\begin{bmatrix}u_{jx}-u_{j-1x}\\ u_{jy}-u_{j-1y}\\ 0\end{bmatrix}+\begin{bmatrix}-\theta_j d_{jy}^{(V_j)}+\theta_{j-1} d_{jy}^{(V_{j-1})}\\ \theta_j d_{jx}^{(V_j)}-\theta_{j-1} d_{jx}^{(V_{j-1})}\\ 0\end{bmatrix}\right),\quad j=2,3, \tag{16}$$

$$\begin{bmatrix}\Delta\xi_4\\ \Delta\eta_4\\ 0\end{bmatrix}=\mathbf{A}_4\left(\begin{bmatrix}-u_{3x}\\ -u_{3y}\\ 0\end{bmatrix}+\begin{bmatrix}\theta_3 d_{4y}^{(V_3)}\\ -\theta_3 d_{4x}^{(V_3)}\\ 0\end{bmatrix}\right), \tag{17}$$

where $\mathbf{A}_i\in R^{3\times3}$ is the coordinate transformation matrix from the inertial frame $Oxyz$ into the hinge frame $O_i\xi_i\eta_i\zeta_i$ determined by:

$$\mathbf{A}_i=\begin{bmatrix}\cos\alpha_i & \sin\alpha_i & 0\\ -\sin\alpha_i & \cos\alpha_i & 0\\ 0 & 0 & 1\end{bmatrix},\ i=1,\ldots,4. \tag{18}$$

Based on the PRB model shown in Fig. 5, the potential energy of the considered compliant mechanism can be determined by the following expression:

$$\Pi=\frac{1}{2}k_R\theta_1^2+\frac{1}{2}\sum_{j=2}^{3}k_R\left(\theta_j-\theta_{j-1}\right)^2+\frac{1}{2}k_R\theta_3^2+\frac{1}{2}\sum_{i=1}^{4}k_{L1}\Delta\xi_i^2+\frac{1}{2}\sum_{i=1}^{4}k_{L2}\Delta\eta_i^2. \tag{19}$$

Introducing a column matrix $\mathbf{q}=\left[q_1,\ldots,q_9\right]^T$ as the vector of generalized coordinates, where $q_{3i-2}=u_{ix}(i=1,\ldots,3)$, $q_{3i-1}=u_{iy}(i=1,\ldots,3)$, and $q_{3i}=\theta_i(i=1,\ldots,3)$, the expression (19) can be written in the following matrix form:

$$\Pi=\frac{1}{2}\mathbf{q}^T\mathbf{K}\mathbf{q} \tag{20}$$

where $\mathbf{K}\in R^{9\times9}$ is the stiffness matrix of the PRB model of the compliant mechanism whose components are given as:

$$K_{ik}=\frac{\partial^2\Pi}{\partial q_i\partial q_k},\ i,k=1,\ldots,9. \tag{21}$$

Using the principle of virtual work as it is shown in [17], in an equilibrium configuration of the compliant mechanism corresponding to an active external static load one has that:

$$-\mathbf{K}\mathbf{q}+\mathbf{Q}=\mathbf{0}_{9\times1}, \tag{22}$$

where, in the considered case, $\mathbf{Q}=\left[\mathbf{F}_1^T,\mathbf{F}_2^T,\mathbf{F}_3^T\right]^T\in R^{9\times1}$ and $\mathbf{0}_{9\times1}\in R^{9\times1}$ is a zero-column matrix. Solving the matrix equation (22) for the column matrix $\mathbf{q}$ yields:

$$\mathbf{q}=\mathbf{K}^{-1}\mathbf{Q}. \tag{23}$$

Finally, based on (23), the parasitic displacements of the lumped compliant parallel-guiding mechanism analysed are given as follows:

$$s_y=u_{2y}\equiv q_5,\quad \theta_p=\theta_2\equiv q_6, \tag{24}$$

whereas the guiding displacement of the mechanism is defined as:

$$s_x=u_{2x}\equiv q_4. \tag{25}$$

The expressions (24) and (25) in the expanded form read:

$$s_y=\frac{2F(2L_c+L_r+2p)(d+t_r)}{d^2k_{L1}+4k_R},\qquad \theta_p=-\frac{4F(2L_c+L_r+2p)}{d^2k_{L1}+4k_R}, \tag{26}$$

$$s_x = \frac{Fd^2 k_{L1}\left[4k_R + k_{L2}(L_c + L_r)^2\right] + 16Fk_R^2 + 4Fk_R k_{L2}\left[5L_c^2 + 6L_c L_r + 2L_r^2 + 4p(2L_c + L_r) + 4p^2\right]}{2k_{L2}k_R(d^2 k_{L1} + 4k_R)}. \quad (27)$$

The expressions (26) and (27) can be applied to any type of flexure hinges with transverse and axial symmetry axes. For example, for the leaf spring type of flexure hinges shown in Fig. 6 one has:

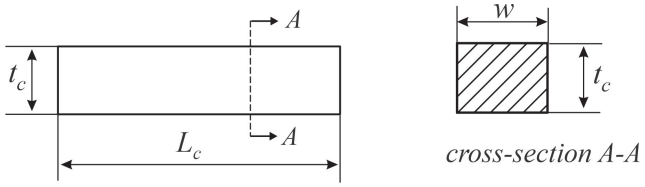

Figure 6: A leaf spring flexure hinge

$$k_R = \frac{EI_c}{L_c}, \quad k_{L1} = \frac{EA_c}{L_c}, \quad k_{L2} = \frac{12A_c EI_c}{A_c L_c^3 + 24I_c L_c \alpha_f (1+\mu)} \quad (28)$$

where $A_c = t_c w$ is the cross-sectional area and $I_c = wt_c^3/12$ is the cross-sectional moment of inertia of the leaf flexure hinge. Now, introducing (28) into (26) and (27) yields:

$$s_y = \frac{2FL_c(2L_c + L_r + 2p)(d + t_r)}{E(A_c d^2 + 4I_c)}, \qquad \theta_p = -\frac{4FL_c(2L_c + L_r + 2p)}{E(A_c d^2 + 4I_c)}, \quad (29)$$

$$s_x = \frac{FL_c A_c d^2(4L_c^2 + 6L_c L_r + 3L_r^2)}{6EI_c(A_c d^2 + 4I_c)} + \frac{4FL_c\alpha_f(1+\mu)}{A_c E} + \frac{4FL_c I_c\left[8L_c^2 + 9L_c L_r + 3L_r^2 + 6p(2L_c + L_r) + 6p^2\right]}{3EI_c(A_c d^2 + 4I_c)}. \quad (30)$$

For $p = 0$ and $\alpha_f = 0$, the expressions (29) and (30) are reduced to the corresponding expressions derived in [33] (see the expressions (24) and (28) in [33]). In this sense, the expressions (29) and (30) represent the generalized forms of the mentioned expressions derived in [33] because these expressions allow the geometric parameter p and the shearing effect during deformations of the flexure hinges to be included in the kinetostatic analysis of the compliant mechanism.

2.2. Model 2

Often, due to the need for a more accurate analysis, it is necessary to take into account the compliances of bodies (V_1) and (V_3) of the compliant mechanism. In order to be able to apply the PRB approach from Section 2.1 in such cases, the bodies (V_1) and (V_3) will further be modeled as two identical leaf spring flexure hinges. According to this, a new PRB model of the lumped compliant parallel-guiding mechanism (model 2) is formed as it is shown in Fig. 7.

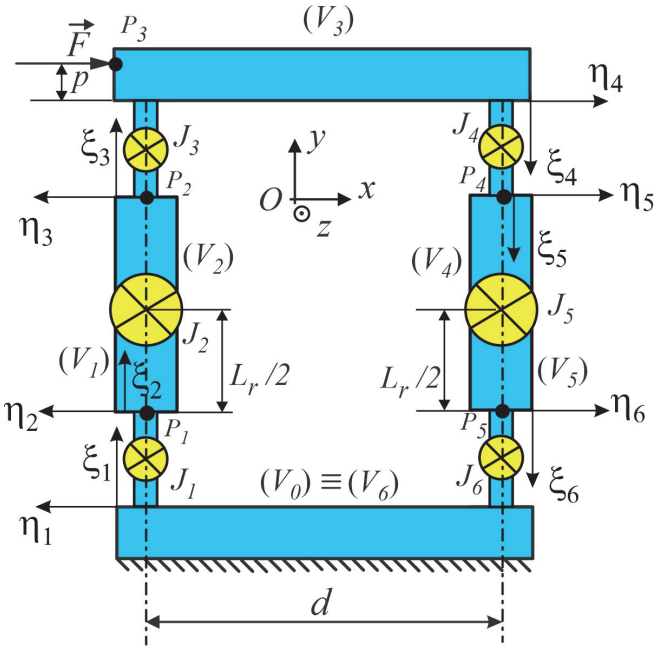

Figure 7: PRB model (model 2) of the lumped compliant parallel-guiding mechanism

Based on Fig. 7, the geometric parameters of the new PRB model (model 2) read:

$$\alpha_1=\alpha_2=\alpha_3=\pi/2,\quad \alpha_4=\alpha_5=\alpha_6=-\pi/2, \tag{31}$$

$$\mathbf{d}_1^{(V_1)}=[0,-\frac{L_c}{2},0]^T,\quad \mathbf{d}_2^{(V_1)}=[0,\frac{L_r}{2},0]^T,\quad \mathbf{d}_2^{(V_2)}=[0,-\frac{L_r}{2},0]^T, \tag{32}$$

$$\mathbf{d}_3^{(V_2)}=[0,\frac{L_c}{2},0]^T,\quad \mathbf{d}_3^{(V_3)}=[\frac{t_r}{2},-p-\frac{L_c}{2},0]^T,\quad \mathbf{d}_4^{(V_3)}=[\frac{t_r}{2}+d,-\frac{L_c}{2}-p,0]^T, \tag{33}$$

$$\mathbf{d}_4^{(V_4)}=[0,\frac{L_c}{2},0]^T,\quad \mathbf{d}_5^{(V_4)}=[0,-\frac{L_r}{2},0]^T,\quad \mathbf{d}_5^{(V_5)}=[0,\frac{L_r}{2},0]^T,\quad \mathbf{d}_6^{(V_5)}=[0,-\frac{L_c}{2},0]^T. \tag{34}$$

According to (28), the stiffnesses $k_{R(j)}, k_{L1(j)}, k_{L2(j)}\,(j=2,5)$ corresponding to joints J_2 and J_5 are determined by:

$$k_{R(j)}=k_R^r=\frac{EI_r}{L_r},\quad k_{L1(j)}=k_{L1}^r=\frac{EA_r}{L_r},\quad k_{L2(j)}=k_{L2}^r=\frac{12A_rEI_r}{A_rL_r^3+24I_rL_r\alpha_f(1+\mu)},\quad j=2,5 \tag{35}$$

where $A_r=t_rw$ is the cross-sectional area and $I_r=wt_r^3/12$ is the cross-sectional moment of inertia of bodies (V_1) and (V_3) shown in Fig. 1. The corresponding active external loads vectors read:

$$\mathbf{F}_1=\mathbf{F}_2=\mathbf{F}_4=\mathbf{F}_5=[0,0,0]^T,\quad \mathbf{F}_3=[2F,0,0]^T, \tag{36}$$

whereas the relative joints displacements are defined as follows:

$$\begin{bmatrix}\Delta\xi_1\\ \Delta\eta_1\\ 0\end{bmatrix}=\mathbf{A}_1\left(\begin{bmatrix}u_{1x}\\ u_{1y}\\ 0\end{bmatrix}+\begin{bmatrix}-\theta_1d_{1y}^{(V_1)}\\ \theta_1d_{1x}^{(V_1)}\\ 0\end{bmatrix}\right), \tag{37}$$

$$\begin{bmatrix}\Delta\xi_j\\ \Delta\eta_j\\ 0\end{bmatrix}=\mathbf{A}_j\left(\begin{bmatrix}u_{jx}-u_{j-1x}\\ u_{jy}-u_{j-1y}\\ 0\end{bmatrix}+\begin{bmatrix}-\theta_jd_{jy}^{(V_j)}+\theta_{j-1}d_{jy}^{(V_{j-1})}\\ \theta_jd_{jx}^{(V_j)}-\theta_{j-1}d_{jx}^{(V_{j-1})}\\ 0\end{bmatrix}\right),\quad j=2,\ldots,5, \tag{38}$$

$$\begin{bmatrix}\Delta\xi_6\\ \Delta\eta_6\\ 0\end{bmatrix}=\mathbf{A}_6\left(\begin{bmatrix}-u_{5x}\\ -u_{5y}\\ 0\end{bmatrix}+\begin{bmatrix}\theta_5d_{6y}^{(V_5)}\\ -\theta_5d_{6x}^{(V_5)}\\ 0\end{bmatrix}\right), \tag{39}$$

and, according to this, the potential energy of the compliant mechanism represented by the model 2 reads:

$$\Pi=\frac{1}{2}k_{R(1)}\theta_1^2+\frac{1}{2}\sum_{j=2}^{5}k_{R(j)}\left(\theta_j-\theta_{j-1}\right)^2+\frac{1}{2}k_{R(6)}\theta_5^2+\frac{1}{2}\sum_{i=1}^{6}k_{L1(i)}\Delta\xi_i^2+\frac{1}{2}\sum_{i=1}^{6}k_{L2(i)}\Delta\eta_i^2 \tag{40}$$

where $k_{R(n)}=k_R, k_{L1(n)}=k_{L1}, k_{L2(n)}=k_{L2}, n=\{1,3,4,6\}$. Similarly, as in Section 2.1, in an equilibrium configuration of the compliant mechanism corresponding to the active external static load shown in Fig. 7 one has that:

$$\mathbf{q}=\mathbf{K}^{-1}\mathbf{Q} \tag{41}$$

where $\mathbf{q}=\left[q_1,\ldots,q_{15}\right]^T, q_{3i-2}=u_{ix}(i=1,\ldots,5), q_{3i-1}=u_{iy}(i=1,\ldots,5), q_{3i}=\theta_i(i=1,\ldots,5)$, $\mathbf{Q}=\left[\mathbf{F}_1^T,\ldots,\mathbf{F}_5^T\right]^T\in R^{15\times1}$, $\mathbf{K}\in R^{15\times15}$, $K_{ik}=\partial^2\Pi/\partial q_i\partial q_k\,(i,k=1,\ldots,15)$. Finally, in the case of the model 2, the guiding displacement s_x and the parasitic displacements s_y and θ_p are defined as:

$$s_x=u_{3x}\equiv q_7,\quad s_y=u_{3y}\equiv q_8,\quad \theta_p=\theta_3\equiv q_9, \tag{42}$$

or, in the expanded form:

$$s_x=\frac{2F}{k_{L2}}+\frac{F}{k_{L2}^r}+\frac{d^2Fk_{L1}k_{L1}^r\left[2k_R^r(L_c+L_r)^2+k_R(L_c^2+L_r^2)\right]}{2k_R\left[4(k_{L1}+2k_{L1}^r)k_Rk_R^r+d^2k_{L1}k_{L1}^r(k_R+2k_R^r)\right]}$$

$$+\frac{F(k_{L1}+2k_{L1}^r)\left[k_R(2L_c+L_r+2p)^2+2k_R^r(5L_c^2+6L_cL_r+2L_r^2+8L_cp+4L_rp+4p^2)\right]+Fk_{L1}d^2k_{L1}^rL_cL_r}{4(k_{L1}+2k_{L1}^r)k_Rk_R^r+d^2k_{L1}k_{L1}^r(k_R+2k_R^r)}, \tag{43}$$

$$s_y=\frac{F(k_{L1}+2k_{L1}^r)(k_R+2k_R^r)(2L_c+L_r+2p)(d+t_r)}{4(k_{L1}+2k_{L1}^r)k_Rk_R^r+d^2k_{L1}k_{L1}^r(k_R+2k_R^r)}, \tag{44}$$

$$\theta_p=-\frac{2F(k_{L1}+2k_{L1}^r)(k_R+2k_R^r)(2L_c+L_r+2p)}{4(k_{L1}+2k_{L1}^r)k_Rk_R^r+d^2k_{L1}k_{L1}^r(k_R+2k_R^r)}. \tag{45}$$

3. NUMERICAL EXAMPLES

3.1. Example 1

In this numerical example the following material and geometric characteristics of the compliant mechanism will be used: mass density $\rho=7820\text{kg/m}^3$, Young's modulus $E=211\times10^9\text{N/m}^2$, Poisson's ratio $\mu=0.288$, $L_c=10\text{mm}$, $L_r=50\text{mm}$, $w=12\text{mm}$, $t_c=0.9\text{mm}$, $t_p=4.5\text{mm}$, $t_r=16\text{mm}$. The model 1 is used. Now we will first analyze the influence of the geometric parameter d on the values of the displacements s_x, s_y, and θ_p. For this purpose let us consider three types of flexure hinges: the leaf spring flexure hinge (see Fig. 6), the right-circular flexure hinge (see Fig. 8(a) where $R=L_c/2$), and the elliptical flexure hinge (see Fig. 8(b) where $a=L_c/2$).

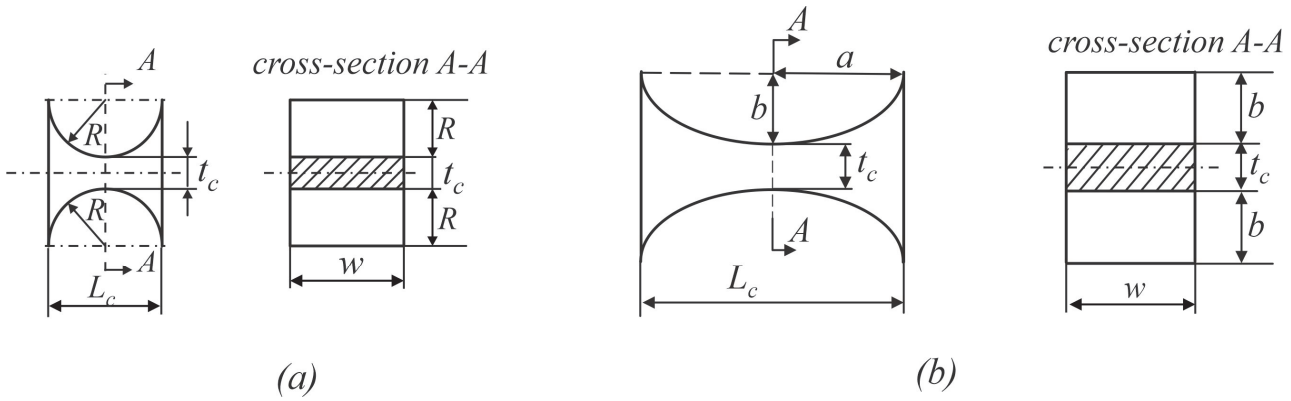

Figure 8: (a) a right-circular flexure hinge; (b) an elliptical flexure hinge

For $p=0$ and $F=5\text{N}$, the corresponding graphs are shown in Figs. 9, 10, and 11. By observing Figs. 9, 10, and 11 it can be concluded that the effect of the parameter d on the guiding displacement s_x is weak. Of course, this conclusion is valid under the assumption that the guiding plate represents a rigid body. Also, increase of d causes a decrease of values of the parasitic displacements s_y and θ_p. Compared to the leaf spring flexure hinge, values of the parasitic displacements are significantly lower in the case of the right-circular and elliptic flexure hinges. This is especially pronounced with the right-circular flexure hinges.

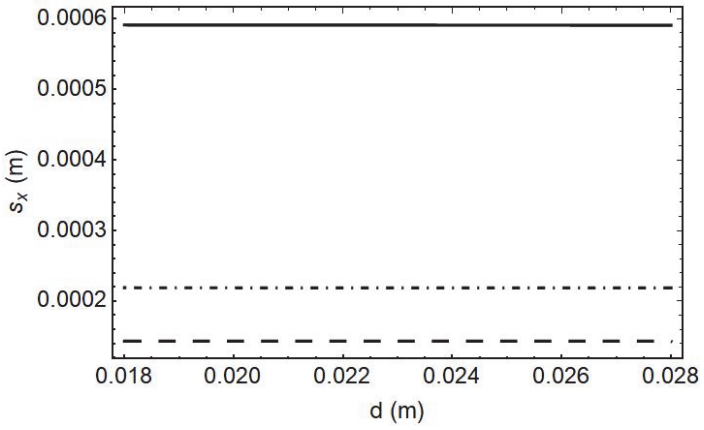

Figure 9: The displacement s_x versus d for three types of flexure hinges: the leaf spring type (solid line); the elliptical type (dot-dash line); the right-circular type (dashed line)

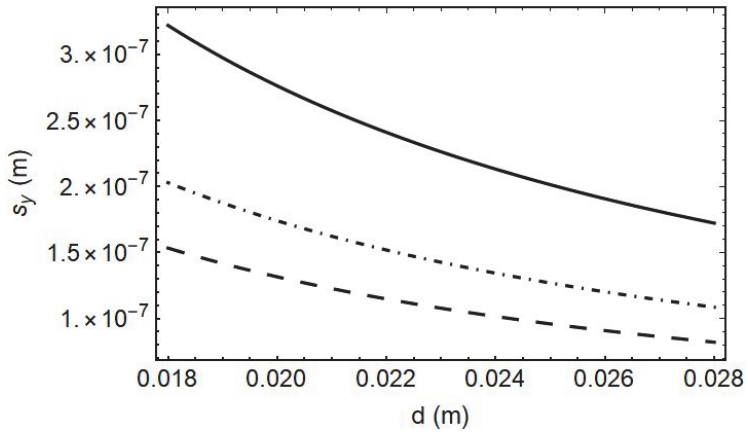

Figure 10: The displacement s_y versus d for three types of flexure hinges: the leaf spring type (solid line); the elliptical type (dot-dash line); the right-circular type (dashed line)

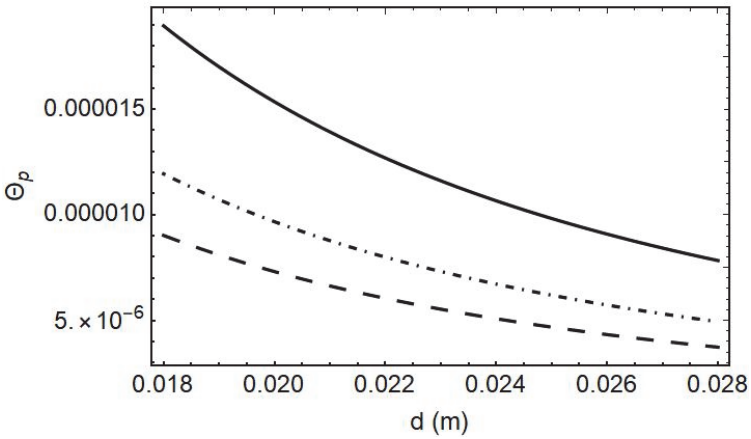

Figure 11: The parasitic angle θ_p versus d for three types of flexure hinges: the leaf spring type (solid line); the elliptical type (dot-dash line); the right-circular type (dashed line)

Finally, for $d = 28\text{mm}$ and $F = 5\text{N}$, the corresponding graphs that characterize the influence of the geometric parameter p on the guiding displacement s_x as well as the parasitic displacements s_y and θ_p are shown in Figs. 12, 13, and 14. Note that the interval $0 \le p \le t_p$ is considered.

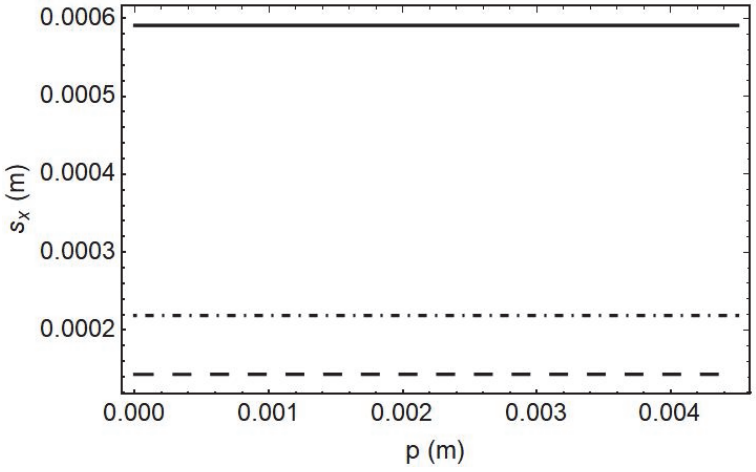

Figure 12: The displacement s_x versus p for three types of flexure hinges: the leaf spring type (solid line); the elliptical type (dot-dash line); the right-circular type (dashed line)

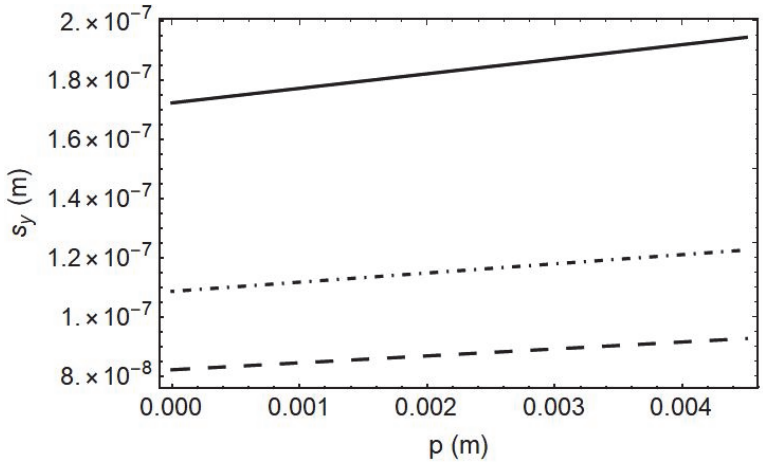

Figure 13: The displacement s_y versus p for three types of flexure hinges: the leaf spring type (solid line); the elliptical type (dot-dash line); the right-circular type (dashed line)

Figs. 13 and 14 clearly show that increasing the parameter p causes an increase in the value of parasitic displacements s_y and θ_p. These values are the least in the case of the right-circular type of flexure hinges. Figure 12 shows that the parameter p has no significant influence on the guiding displacement s_x.

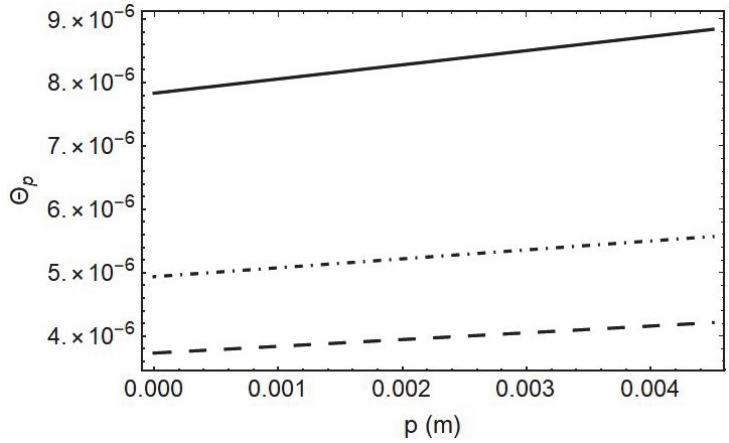

Figure 14: The parasitic angle θ_p versus p for three types of flexure hinges: the leaf spring type (solid line); the elliptical type (dot-dash line); the right-circular type (dashed line)

3.2. Example 2

In this example the PRB model developed in Section 2.2 (called as model 2) will be tested through the comparison with the results obtained in [21,22]. For this purpose, the material and geometric characteristics of the compliant mechanism used in [21,22] will be considered as follows: $E = 200$ GPa, $\mu = 0.288$, $L_c = 6$mm, $L_r = 24$mm, $w = 8$mm $t_c = 0.6$mm, $t_p = 6.6$mm, $t_r = 6.6$mm, $F = 5$N, $p = 0$, $d = 36.6$mm. Using both the approach developed in this paper and the approaches given in [21,22], the values of the angle θ_p and the horizontal and vertical displacements of point P indicated in Fig. 7 are determined and shown in Table 1.

Table 1: Values of the angle θ_p and the horizontal and vertical displacements of point P

Methods	u_{Px} [μm]	u_{Py} [μm]	θ_p
FEM [22]	122.0	0.14	-
PRB approach (model 2)	120.89	0.0415	-2.26936×10^{-6}
Method in [22]	121.2	0.04	-
Method in [21]	118.0	0.00	-

Here, one has that $u_{Px} = s_x$ and $u_{Py} = s_y + (t_r / 2)\theta_p$. By observing data given in Table 1 it is obvious that the PRB approach proposed in this paper gives the results of high accuracy.

4. CONCLUSION

Using PRB approach, the corresponding expressions for parasitic displacements of the lumped compliant parallel-guiding mechanism have been derived. The derived expressions are valid for lumped compliant parallel-guiding mechanisms with both leaf spring flexure hinges and flexure hinges of variable thickness possessing transverse symmetry axis. These expressions include all geometric and physical parameters of the compliant mechanism as well as the shearing effect during deformations of the flexure hinges. This fact makes the derived expressions suitable for solving the problem of minimization of the parasitic displacements. Leaf spring, right-circular, and elliptical flexure hinges have been considered. It has been shown that flexure hinges of variable thickness allow significantly smaller values of the parasitic displacements of lumped compliant parallel-guiding mechanisms compared to the parasitic displacements values that are achieved when leaf spring flexure hinges are used. However, leaf spring flexure hinges enable higher values of the guiding displacement to be achieved. The stiffness coefficients k_{L2} and $k_{L2}^{(r)}$ have no effect on the compliant mechanism parasitic displacements.

ACKNOWLEDGEMENTS

This research was supported by the Ministry of Science, Technological Development, and Innovation of the Republic of Serbia (Grant No. 451-03-47/2023-01/200108). This support is gratefully acknowledged.

REFERENCES

[1] L.L. Howell, "Compliant Mechanisms", John Wiley & Sons, New York (USA), (2001).

[2] L.L. Howell, S.P. Magleby, and B.M. Olsen (editors), "Handbook of Compliant Mechanisms", John Wiley & Sons, Chichester (UK), (2013)

[3] N.D. Pavlović and N.T. Pavlović, "Compliant Mechanisms", Faculty of Mechanical Engineering, University of Niš, Niš (Serbia), (2013)

[4] L. Zentner and S. Linβ, "Compliant Systems – Mechanics of Elastically Deformable Mechanisms, Actuators and Sensors", De Gruyter, Oldenbourg, Muenchen (Germany), (2019)

[5] N. Lobontiu, "Compliant Mechanisms: Design of Flexure Hinges", CRC Press, Boca Raton (USA), (2021).

[6] J. Hu, T. Wen, and J. He, "Dynamics of compliant mechanisms using transfer matrix method", Int. J. Precis. Eng., Vol. 21(11), pp. 2173-2189, https://doi.org/10.1007/s12541-020-00395-9, (2020)

[7] M. Ling, L. Yuan, J. Lai, H. Wei, and X. Zhang, "Compliance and precision modeling of general notch flexure hinges using a discrete-beam transfer matrix", Precis. Eng., Vol. 82, pp. 233-250, https://doi.org/10.1016/j.precisioneng.2023.03.014, (2023)

[8] M. Ling, L. Yuan, and X. Zhang, "Static and dynamic compliance analyses of curved-axis flexure hinges: A discrete beam transfer matrix", J. Mech. Des., Vol. 145(6), p. 064501, https://doi.org/10.1115/1.4056757, (2023)

[9] M. Ling, L. Yuan, H. Zhou, and M. Ning, "Modified transfer matrix method for vibration analysis of beam structures including branches and rigid bodies", Mech. Syst. Signal Process., Vol. 187, p. 109858, https://doi.org/10.1016/j.ymssp.2022.109858, (2023)

[10] L. Yuan, M. Ling, J. Lai, H. Li, and X. Zhang, "Graphic transfer matrix method for kinetostatic and dynamic analyses of compliant mechanisms", J. Mech. Des., Vol. 16(2), p. 021009, https://doi.org/10.1115/1.4056827, (2024)

[11] M. Ling, X. Zhang, and J. Cao, "Extended dynamic stiffness model for analyzing flexure- hinge mechanisms with lumped compliance", J. Mech. Des., Vol. 144(1), p. 013304, https://doi.org/10.1115/1.4051891, (2022)

[12] M. Ling, H. Zhou, and L. Chen, "Dynamic stiffness matrix with Timoshenko beam theory and linear frequency solution for use in compliant mechanisms", J. Mechanisms Robotics, Vol. 15(6), p. 061002, https://doi.org/10.1115/1.4056236, (2023)

[13] S. Henning and L. Zentner, "Analysis of planar compliant mechanisms based on non-linear analytical modeling including shear and lateral contraction", Mech. Mach. Theory, Vol. 164, p. 104397, https://doi.org/10.1016/j.mechmachtheory.2021.104397, (2021)

[14] V. Platl and L. Zentner, "An analytical method for calculating the natural frequencies of spatial compliant mechanisms", Mech. Mach. Theory, Vol. 175, p. 104939, https://doi.org/10.1016/j.mechmachtheory.2022.104939, (2022)

[15] S. Henning and L. Zentner, "Analytical characterization of spatial compliant mechanisms using beam theory In: Pandey, A.K., Pal, P., Nagahanumaiah, Zentner, L. (eds) Microactuators, Microsensors and Micromechanisms. MAMM 2022. Mechanisms and Machine Science, vol 126. Springer, Cham. https://link.springer.com/chapter/10.1007/978-3-031-20353-4_5, (2023)

[16] N. Li, H.J. Su, and X.P. Zhang "Accuracy assessment of pseudo-rigid-body model for dynamic analysis of compliant mechanisms", J. Mechanisms Robotics, Vol. 9(5), p. 054503, https://doi.org/10.1115/1.4037186, (2017).

[17] S. Šalinić and A. Nikolić, "A new pseudo-rigid-body model approach for modeling the quasi-static response of planar flexure-hinge mechanisms", Mech. Mach. Theory, Vol. 124, pp. 150-161, https://doi.org/10.1016/j.mechmachtheory.2018.02.011, (2018)

[18] Y.Q. Yu, P. Zhou, and Q.P. Xu, "Kinematic and dynamic analysis of compliant mechanisms considering both lateral and axial deformations of flexural beams", Proc. Inst. Mech. Eng. C: J. Mech. Eng. Sci., Vol. 233(3), pp. 1007-1020, https://doi.org/10.1177/0954406218760956, (2019)

[19] H. Xu, J. Gan, and X. Zhang, "A generalized pseudo-rigid-body PPRR model for both straight and circular beams in compliant mechanisms", Mech. Mach. Theory, Vol. 154, p. 104054, https://doi.org/10.1016/j.mechmachtheory.2020.104054, (2020)

[20] H. Xu, X. Zhang, R. Wang, H. Zhang, and J. Liang, "Design of an SMA-driven compliant constant-force gripper based on a modified chained pseudo-rigid-body model", Mech. Mach. Theory, Vol. 187, p. 105371, https://doi.org/10.1016/j.mechmachtheory.2023.105371, (2023)

[21] Y. Shen, X. Chen, W. Jiang, and X. Luo, "Spatial force-based non-prismatic beam element for static and dynamic analyses of circular flexure hinges in compliant mechanisms", Precis. Eng., Vol. 38(2), pp. 311-320, https://doi.org/10.1016/j.precisioneng.2013.11.001, (2014)

[22] M. Ling, J. Cao, Z. Jiang, and J. Lin, "A semi-analytical modeling method for the static and dynamic analysis of complex compliant mechanism", Precis. Eng., Vol. 52, pp. 64-72, https://doi.org/10.1016/j.precisioneng.2017.11.008, (2018)

[23] N.T. Pavlović and D. Stojiljković, "Guiding accuracy of the Watt compliant cognate mechanisms", FU Mech. Eng., https://doi.org/10.22190/FUME220822044P, (2023)

[24] H. Lim and Y.M. Choi, "Enhanced generalized modeling method for compliant mechanisms: multi-compliant-body matrix method", Struct. Eng. Mech., Vol. 82(4), pp. 503-515, https://doi.org/10.12989/sem.2022.82.4.503, (2022)

[25] N. Lobontiu, J. Wight-Crask, and C. Kawagley, "Straight-axis folded flexure hinges: in-plane elastic response", Precis. Eng., Vol. 57, pp. 54-63, https://doi.org/10.1016/j.precisioneng.2019.03.006, (2019)

[26] L. Li, D. Zhang, H. Qu, and Y. Wang, "Generalized model and configuration design of multiple-axis flexure hinges", Mech. Mach. Theory, Vol. 169, p. 104677, https://doi.org/10.1016/j.mechmachtheory.2021.104677, (2022)

[27] N. Lobontiu, "Compliance-based matrix method for modeling the quasi-static response of planar serial flexure-hinge mechanisms", Precis. Eng., Vol. 38(3), pp. 639-650, https://doi.org/10.1016/j.precisioneng.2014.02.014, (2014)

[28] W. Tuo, X. Li, Y. Ji, T. Wu, and Z. Xie, "Analytical compliance model for right circle flexure hinge considering the stress concentration effect", Int. J. Precis. Eng. Manuf., Vol. 21(5), pp. 895-904, https://doi.org/10.1007/s12541-019-00306-7, (2020)

[29] H. Wei, B. Shirinzadeh, H. Tang, and X. Niu, "Closed-form compliance equations for elliptic-revolute notch type multiple-axis flexure hinges", Mech. Mach. Theory, Vol. 156, p. 104154, https://doi.org/10.1016/j.mechmachtheory.2020.104154, (2021)

[30] M. Ling, L.L. Howell, J. Cao, and G. Chen, "Kinetostatic and dynamic modeling of flexure-based compliant mechanisms: A survey", Appl. Mech. Rev., Vol. 72(3), p. 030802, https://doi.org/10.1115/1.4045679, (2020)

[31] Z. Ni, D. Zhang, Y. Wu, Y. Tian, and M. Hu, "Analysis of parasitic motion in parallelogram compliant mechanism", Precis. Eng., Vol. 34(1), pp. 133-138, https://doi.org/10.1016/j.precisioneng.2009.05.001, (2010)

[32] X. Yang, W. Li, Y. Wang, and G. Ye, "Output displacement analysis for compliant single parallel four-bar mechanism", Proceedings of the 2010 IEEE International Conference on Mechatronics and Automation, Xi'an (China), August 4-7, 2010, pp. 1354-1357, https://doi.org/10.1109/ICMA.2010.5588308, (2010)

[33] L. Yuanqiang, L. Wangyu, and W. Lei, "Analysis of the displacement of lumped compliant parallel-guiding mechanism considering parasitic rotation and deflection on the guiding plate and rigid beams", Mech. Mach. Theory, Vol. 91, pp. 50-68, https://doi.org/10.1016/j.mechmachtheory.2015.04.007, (2015)

[34] M. Arredondo-Soto, E. Cuan-Urquizo, A. Gómez-Espinosa, A. Roman-Flores, P.D.U. Coronado, and M. Jimenez-Martinez, "The compliant version of the 3-RRR spherical parallel mechanism known as ''Agile-Eye'': Kinetostatic analysis and parasitic displacement evaluation", Mech. Mach. Theory, Vol. 180, p. 105160, https://doi.org/10.1016/j.mechmachtheory.2022.105160, (2023)